

## Measurement of the photon detection inefficiency of electromagnetic calorimeters at energies below 1 GeV

S. Ajimura<sup>a</sup>, K. Arisaka<sup>b</sup>, M. Barrio<sup>c</sup>, T. Fujiwara<sup>d</sup>, S. Hidaka<sup>a</sup>, T. Hotta<sup>a</sup>,  
B. Hsiung<sup>e</sup>, Y. Ikegami<sup>f</sup>, T. Inagaki<sup>f,\*</sup>, S. Kabe<sup>f</sup>, R. Kessler<sup>c</sup>, S. Kobayashi<sup>g</sup>,  
H. Kurashige<sup>d</sup>, K. Kurebayashi<sup>a</sup>, T. Matsumura<sup>a</sup>, T. Miyahara<sup>g</sup>, K. Mori<sup>a,h</sup>,  
T. Nakagawa<sup>g</sup>, T. Nakamura<sup>d</sup>, T. Nakano<sup>a</sup>, T. Nomura<sup>d</sup>, H. Okuno<sup>f</sup>, N. Sasao<sup>d</sup>,  
T. Sato<sup>f</sup>, T. Shinkawa<sup>f,i</sup>, I. Suzuki<sup>a</sup>, A. Tripathi<sup>b</sup>, T. Tsukamoto<sup>g</sup>, Y. Wah<sup>c</sup>,  
H. Watanabe<sup>f,g,\*\*</sup>, B. Winstein<sup>c</sup>, T. Yamanaka<sup>a</sup>

<sup>a</sup>Department of Physics, Osaka University, Toyonaka 560-0043, Osaka, Japan

<sup>b</sup>University of California, Los Angeles 90095, CA, USA

<sup>c</sup>Enrico Fermi Institute, University of Chicago, Chicago 60637, IL, USA

<sup>d</sup>Department of Physics, Kyoto University, Kyoto 606-8502, Kyoto, Japan

<sup>e</sup>Fermi National Accelerator Laboratory, Batavia 60510, IL, USA

<sup>f</sup>High Energy Accelerator Research Organization, KEK, Tsukuba 305-0801, Ibaraki, Japan

<sup>g</sup>Department of Physics, Saga University, Saga 840-8502, Saga, Japan

<sup>h</sup>Department of Applied Physics, University of Miyazaki, Miyazaki 889-2192, Miyazaki, Japan

<sup>i</sup>National Defense Academy in Japan, Yokosuka 239-8686, Kanagawa, Japan

Received 9 June 2005; accepted 27 June 2005

Available online 22 July 2005

---

### Abstract

The photon detection inefficiency of electromagnetic calorimeters due to photonuclear reactions has been studied at photon energies below 1 GeV using a tagged-photon beam at the KEK-Tanashi 1.3-GeV electron synchrotron. Photonuclear reactions are identified by detecting low-energy neutrons with liquid scintillation counters surrounding the sample calorimeter. For a Cesium Iodide (CsI) calorimeter with a detection threshold of 10 MeV, the inefficiency due to photonuclear reactions is  $10^{-4}$  at  $E_\gamma = 100$  MeV, and decreases to  $2 \times 10^{-7}$  at  $E_\gamma = 1$  GeV. For a lead-scintillator sampling calorimeter, the inefficiency is larger than the above values by a factor of 2–3, reflecting the sampling effect

---

\*Corresponding author.

\*\*Corresponding author. High Energy Accelerator Research Organization, KEK, Tsukuba 305-0801, Ibaraki, Japan. Tel.: +81 29 864 5428; fax: +81 29 864 7831.

E-mail addresses: [inagaki@post.kek.jp](mailto:inagaki@post.kek.jp) (T. Inagaki), [nabe@post.kek.jp](mailto:nabe@post.kek.jp) (H. Watanabe).

after photonuclear reactions. By decreasing the detection threshold down to 1 MeV, the inefficiencies are reduced by a factor of 10 for both types of calorimeters.

© 2005 Elsevier B.V. All rights reserved.

PACS: 29.40.Vj

Keywords: Electromagnetic calorimeter; Photon detection inefficiency  $K_L^0 \rightarrow \pi^0 \nu \bar{\nu}$  decay

## 1. Introduction

The detection inefficiency of an electromagnetic (EM) calorimeter for photons is one of the most crucial parameters in the experimental search for the  $K_L^0 \rightarrow \pi^0 \nu \bar{\nu}$  decay [1]. The experimental signature for this decay mode is “ $\pi^0 + \text{nothing}$ ”, where “nothing” means no other visible particles besides the  $\pi^0$  in the final state. In order to confirm nothing, highly efficient veto detectors must surround the  $K_L^0$  decay region. In this experiment, the main background comes from the  $K_L^0 \rightarrow \pi^0 \pi^0$  decay, where two photons are not detected because of the calorimeter inefficiency. Since the ratio of branching ratios,  $B(K_L^0 \rightarrow \pi^0 \nu \bar{\nu})/B(K_L^0 \rightarrow \pi^0 \pi^0)$ , is expected to be  $\sim 10^{-8}$ , the calorimeter inefficiency for a single photon must be smaller than  $10^{-4}$  in order to reduce the  $K_L^0 \rightarrow \pi^0 \pi^0$  background below the signal level.

High-energy photons are absorbed in a calorimeter through EM interactions or photonuclear reactions. The photon detection inefficiency of the calorimeter arises from an event in which the energy deposition in the calorimeter is smaller than the detection threshold. As discussed in a previous paper [2], the following three effects determine the detection inefficiency: (1) punch-through, (2) photonuclear reaction and (3) sampling for sampling calorimeters. Since EM processes are well reproduced by a simulation, and are dominant in photon absorption, the punch-through rate and the sampling effect can be estimated by the EGS [3] simulation codes. However, since there is no realistic simulation code for evaluating the detection inefficiency for photonuclear reactions, this effect should be studied experimentally.

In a previous paper [2], we reported on a new method to measure the photon inefficiency of a

calorimeter due to photonuclear reactions. In the photon energy region between 185 and 505 MeV, results were presented for an undoped Cesium Iodide (CsI) calorimeter and for a lead-scintillator (2 mm/6 mm) sampling calorimeter. In an upgraded experiment reported here, we apply the same method to various types of calorimeters over a wider energy region from 100 MeV to 1 GeV.

## 2. Experimental method and apparatus

### 2.1. Overview

The experimental method is similar to that in our previous experiment [2]. Since the photon inefficiency from photonuclear reactions is between  $10^{-7}$  and  $10^{-4}$ , a direct measurement would require exceptional photon tagging efficiency that is not feasible. Therefore, we took a different approach to achieve this accuracy. The experimental setup is shown in Fig. 1, where a collimated tagged-photon beam impinges on a sample calorimeter placed 4.7 m downstream of the photon radiator. In the sample calorimeter, a photon with a known energy is absorbed through EM interactions or through photonuclear reactions, and deposits energy in the calorimeter. When the photon is absorbed through photonuclear reactions, it is expected that low energy neutrons are emitted from the nucleus together with charged particles. These neutrons emerge outside of the calorimeter. We identify the photonuclear reaction by requiring the detection of one or more neutrons in a liquid scintillator (LS) detector surrounding the sample calorimeter. There are 12 LS detectors as shown in Fig. 2. For these events with neutrons identified in the LS (“LS-neutron” events), we also measure the calorimeter response.

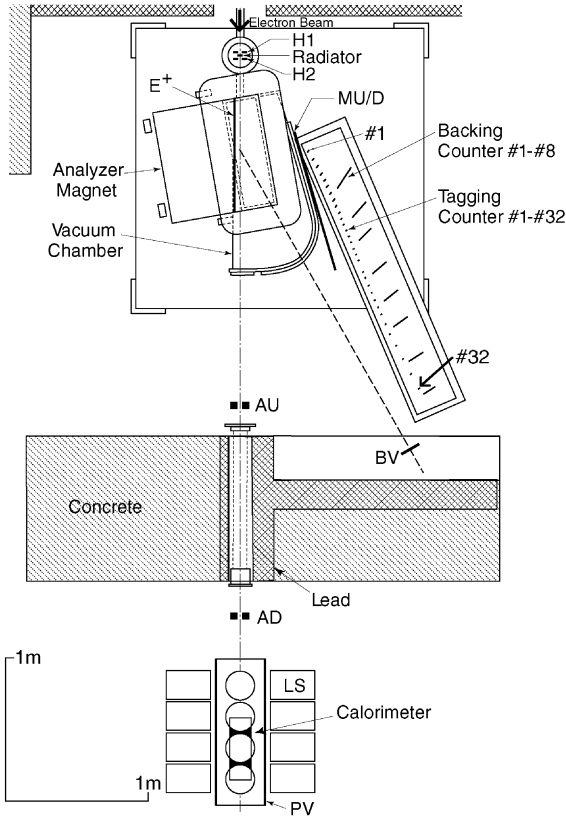


Fig. 1. Plan view of the experimental setup.

## 2.2. Tagged-photon beam

An electron beam from the electron synchrotron hits a thin platinum radiator and produces photons via bremsstrahlung. The energy of the scattered electron is analyzed by a magnetic spectrometer in the energy range from 100 to 420 MeV with an energy bin of 10 MeV. The electron momentum is determined from a hodoscope with 32 “tagging counters” placed along the focal line of the magnet with respect to the radiator. To reduce accidentals, there is an additional hodoscope with 8 backing counters, each covering four tagging counters. Thus, the tagged-photon energy ( $E_\gamma$ ) is  $E_\gamma = E_e - E_{e'}$ , where  $E_e$  is the incident electron energy and  $E_{e'}$  is the scattered electron energy. For this experiment, we set  $E_e = 430, 750$  and  $1100$  MeV, which cover the

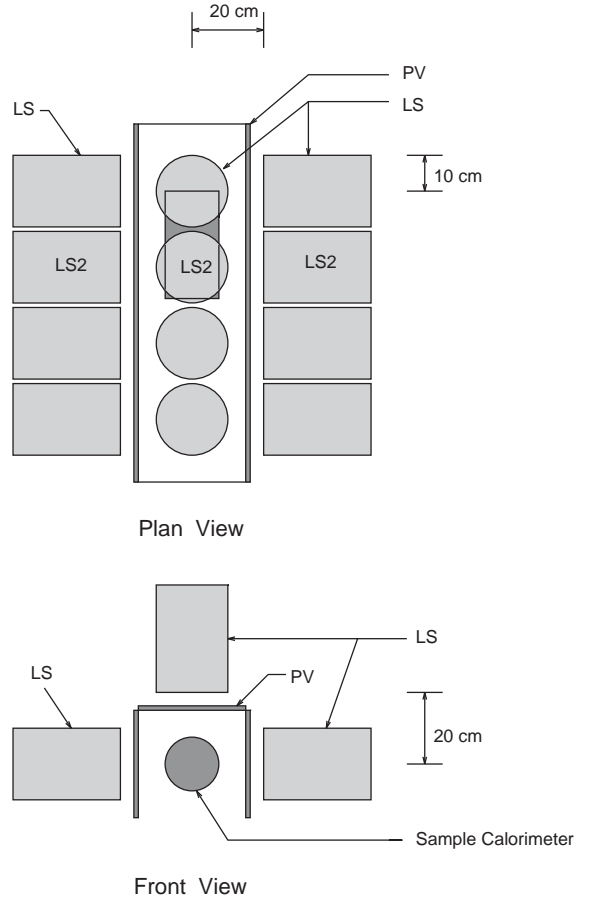


Fig. 2. Detector configuration of the calorimeter and the liquid-scintillation counters. The “LS” in the figure shows the liquid-scintillation counter and the “PV” shows the plastic-scintillation counter for charged-particle veto. LS2 in the figure shows 2nd layer LS’s counting from upstream.

$E_\gamma$  range below 1 GeV. Details of the photon tagging system are described elsewhere [4,5].

For this inefficiency measurement, a high-purity tagged photon beam is important. If a photon produced in the radiator pair-produces (to  $e^+e^-$ ) before leaving the radiator, a tagging-counter hit will not be associated with a photon. These “mis-tag” events are reduced with a thinner radiator at the expense of fewer tagged photons; the optimized thickness was chosen to be  $0.02 X_0$  at  $E_e = 430$  MeV and  $0.04 X_0$  at 750 and 1100 MeV. Veto counters in the photon tagging system, as explained in [2], further reduced mis-tags. Two active

collimators, AU and AD, define the cross section of the tagged photon beam. AU is a lead-scintillator (1 mm/5 mm) sandwich counter with a 2.5 cm diameter beam hole. AD is an undoped-CsI crystal calorimeter with a 2 cm diameter beam hole. When either of these veto counters has a signal more than three sigma above pedestal, the event is discarded. The fraction of mis-tag events with this system is less than 2%.

### 2.3. Neutron detection

As shown in Fig. 2, 12 modules of liquid-scintillation counters surround the sample calorimeter. The LS is NE213 (Nuclear Enterprise), and is contained in a cylindrical aluminum vessel with 20 cm diameter and 33 cm length. Scintillation light is amplified by a photomultiplier tube (PMT) with 5-in. diameter. This signal is then read out by a LeCroy 2249SG Analog-to-Digital Converter (ADC), and is also fed to a high-resolution Time-to-Digital Converter (TDC) to measure the relative time between the LS signal and the photon-tagging counter. For the timing measurement, a constant-fraction discriminator was used with a threshold of 0.2 MeV-electron-equivalent. Three long plastic scintillator bars (PV) are placed in front of the LS modules to veto charged particles incident on the LS.

Separation between neutrons and photons is based on the slower time-of-flight (TOF) for the neutrons, and on signals obtained in both a narrow 35 ns ADC gate and in a wide 200 ns gate; the signal fraction in the 35 ns gate is larger for photons. The gain was calibrated by using the isotopes  $^{60}\text{Co}$  and  $^{241}\text{Am/Be}$ .

The main improvement in the current measurement (compared to [2]) is the addition of a TOF measurement between the calorimeter and the LS, and a pulse-shape ADC measurement with two separate gates. Our previous measurement used only a Pulse-Shape-Discriminator (CAMBERA-2160) for neutron identification.

### 2.4. Calorimeter samples

Two types of EM calorimeters were prepared for inefficiency measurements: (a) undoped-CsI calorimeters and (b) lead-scintillator sampling calorimeters. The parameters of the CsI and sampling calorimeters are listed in Tables 1 and 2, respectively.

For the undoped CsI calorimeter, two different geometries were used: CsI-(I) and CsI-(II), as shown in Figs. 3 and 4. CsI-(I) was used in our previous experiment [2]. This calorimeter has a cylindrical shape consisting of 10 tightly packed modules. The radius is 7.4 cm (2.1 Moliere radius) and the length is 30 cm (16.2  $X_0$ ). Scintillation light from the central crystal was read out by a 2-in. PMT, and each peripheral crystal was read out by a 1 $\frac{1}{8}$ -in. PMT.

CsI-(II) is a  $3 \times 3$  matrix, each having a square cross section of  $5 \times 5 \text{ cm}^2$  and a length of 50 cm (27  $X_0$ ). These crystals are spares from the KTeV experiment [6]. Scintillation light from each crystal was read out by a 1.5-in. PMT.

The lead-scintillator sampling calorimeter was also prepared with two different geometries: SC-(I) and SC-(II), as shown in Figs. 5 and 6. SC-(I) is composed of 81 layers of 1 mm thick lead plates alternating with 82 layers of 3 mm thick plastic scintillator plates. This module has a hexagonal

Table 1  
Parameters of undoped-CsI crystal calorimeters

Calorimeter	Cross-section ( $\text{cm}^2$ )	Length		
		Total length ( $L$ ) (cm)	Total radiation length ( $L/X_0$ )	Total nuclear interaction length ( $L/\lambda_I$ )
CsI-(I)	$\pi \times 7.4^2$	30.0	16.7	0.814
CsI-(II)	$15.0 \times 15.0$	50.0	27.0	1.36

The  $\pi \times 7.4^2$  means cylindrical shape with *radius* = 7.4 cm.

Table 2  
Parameters of lead-scintillator sampling calorimeters

Sampling composition (Lead/scinti.)	Cross-section (cm <sup>2</sup> )	No. of layers (lead)	Length			
			Total length ( $L$ ) (cm)	Total radiation length ( $L/X_0$ )	Total nuclear interaction length ( $L/\lambda_I$ )	$\alpha$ ( $\lambda_I/X_0$ )
1 mm/3 mm	$\sim\pi \times 8.2^2$ (hexagonal shape)	81	$\sim 35$	15	0.782	$5.2 \times 10^{-2}$
1 mm/5 mm (for 1-module)	15.0 $\times$ 15.0	16	$\sim 10$	3.1	0.195	$6.3 \times 10^{-2}$
0.5 mm/5 mm (for 1-module)	15.0 $\times$ 15.0	17	$\sim 10$	1.7	0.158	$9.3 \times 10^{-2}$

The last column,  $\alpha$ , is the ratio of the nuclear interaction length to the radiation length in average.

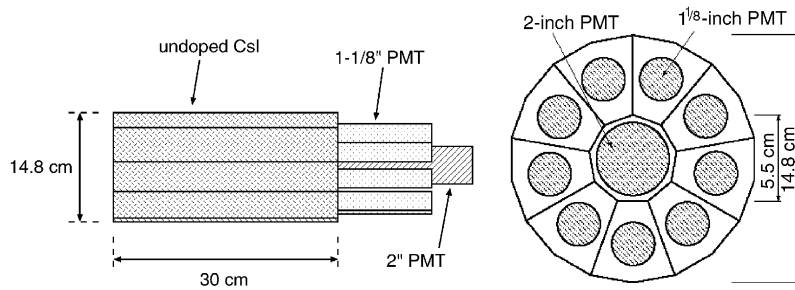


Fig. 3. Side and rear views of the undoped-CsI calorimeter (CsI-I).

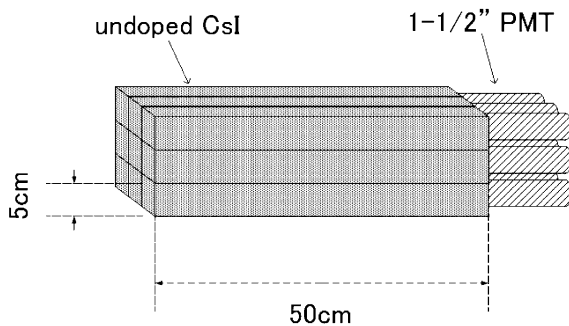


Fig. 4. Schematic view of the undoped-CsI calorimeter using crystals and PMTs from KTeV (CsI-II).

cross-section with a diagonal size of 16.2 cm and a length of about 36 cm ( $15 X_0$ ). Scintillation light is read out by six 2-in. PMT's via wavelength shifter bars placed at the hexagonal peripheries of the module.

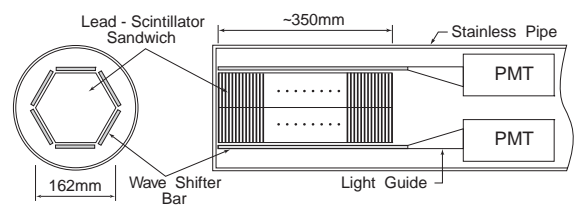


Fig. 5. Front and side views of the 1-mm lead/3-mm scintillator sampling calorimeter (SC-I).

SC-II) has a modular structure and each module has a square-shape cross-section of  $15 \times 15 \text{ cm}^2$  and a length of 10 cm (Fig. 6) with two sampling compositions: 1 mm lead and 5 mm scintillator (16 layers,  $3.1 X_0$  per module), and 0.5 mm lead and 5 mm scintillator (17 layers,  $1.7 X_0$  per module). Scintillation light was read out by a 2-in. PMT through a lucite light guide, as shown

in Fig. 6. For the first sampling calorimeter there are six 1 mm/5 mm modules (Fig. 7). For the second calorimeter there are two 0.5 mm/5 mm

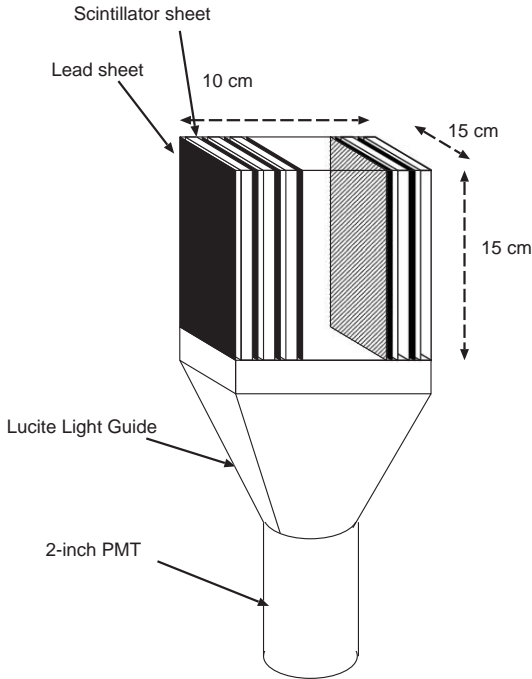


Fig. 6. Schematic view of the unit module (1 mm/5 mm or 0.5 mm/5 mm) of sampling calorimeters (SC-II).

modules followed by six 1 mm/5 mm modules (Fig. 7). This last configuration is used to study the case in which the inefficiency from photo-nuclear reactions arises before the EM shower process. The backing of six 1 mm/5 mm modules reduces punch through.

## 2.5. Trigger logic and DAQ system

Fig. 8 shows diagrams of the trigger and data-acquisition system. The  $\Sigma_{\text{tag}}$  trigger is any coincidence between a tagging-counter signal and the corresponding backing-counter signal. The  $\Sigma_{\text{tag}} \cdot \overline{E_{\text{cal}}}$  trigger is the  $\Sigma_{\text{tag}}$  trigger vetoed by the sample calorimeter signal corresponding to an energy deposition larger than 60–70% of the incident energy. Note that the  $\Sigma_{\text{tag}}$  trigger is used to determine the number of photons incident on the calorimeter, and the  $\Sigma_{\text{tag}} \cdot \overline{E_{\text{cal}}}$  trigger provides the sample used for the inefficiency measurement. A third trigger records accidental activity; it is a coincidence between the  $\Sigma_{\text{tag}}$  signal and the  $E_{\text{cal}}$  signal, in which the  $\Sigma_{\text{tag}}$  signal is delayed by 100  $\mu\text{s}$ . For all of these triggers, the beam-veto counters are used.

We collected data with these three triggers simultaneously. To reduce dead time from the

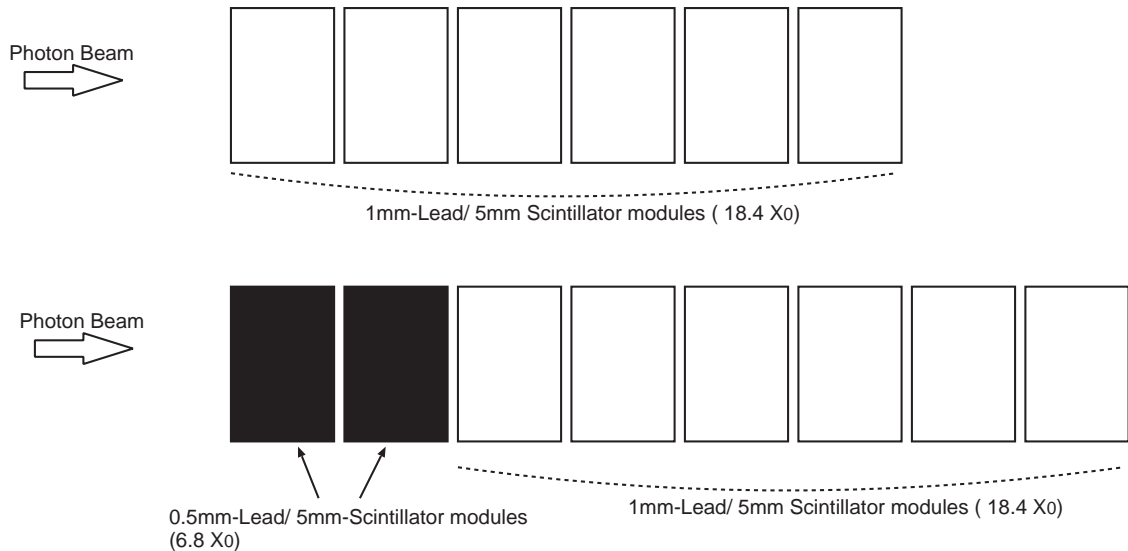


Fig. 7. Schematic view of the experimental setup of SC-II). The top figure shows the setup for the 1-mm lead/5-mm scintillator calorimeter, and the bottom figure shows the setup for the 0.5-mm lead/5-mm scintillator calorimeter.

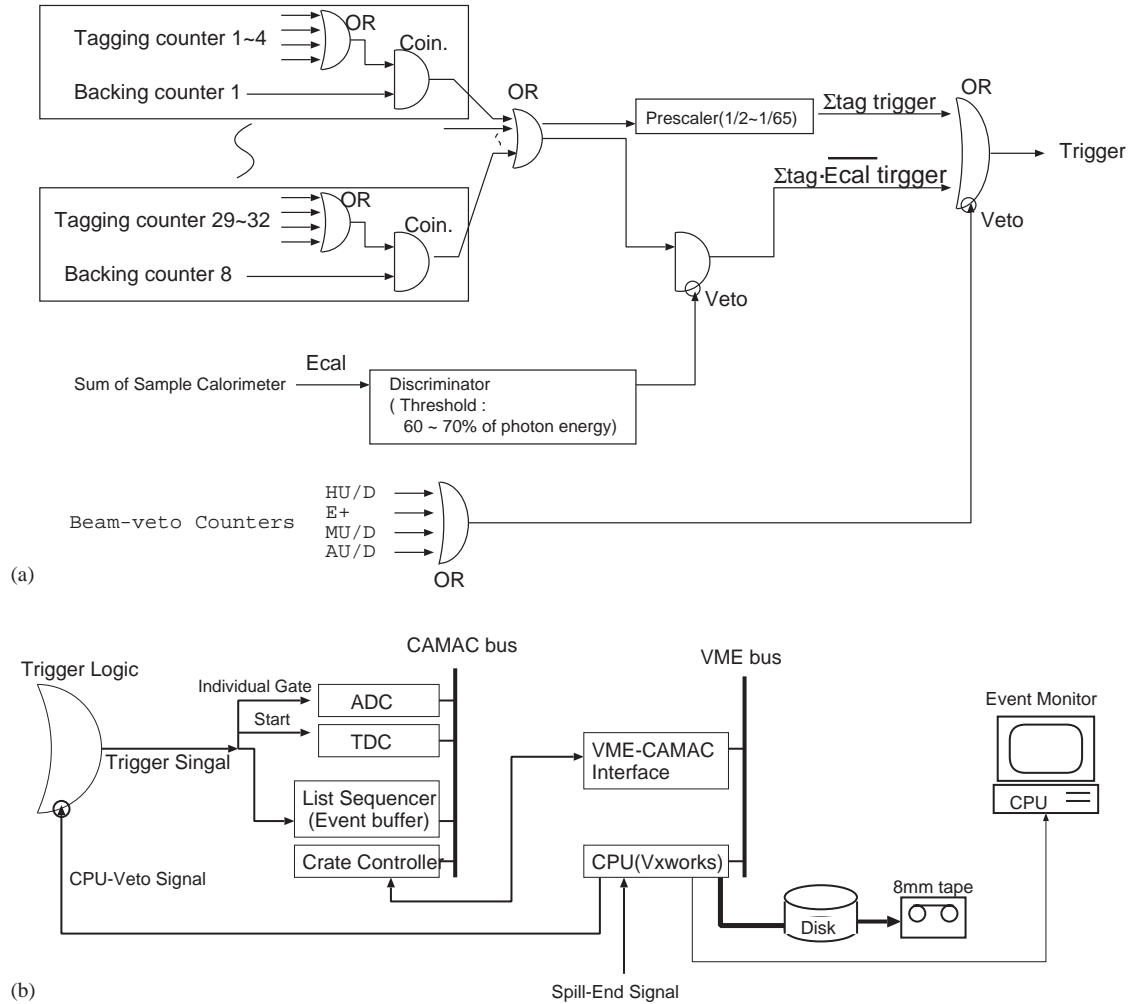


Fig. 8. The top figure shows a logic diagram of the  $\Sigma\text{tag}$  trigger and the  $\Sigma\text{tag} \cdot \overline{E_{\text{cal}}}$  trigger. The bottom figure shows the data-acquisition system (DAQ).

high-rate  $\Sigma\text{tag}$  trigger, this trigger was pre-scaled by a factor between 2 and 65 depending on the incident beam intensity.

The beam-spill duration was typically 5 ms with a repetition rate of 21.5 Hz, and the electron beam intensity was controlled to be  $4.6 \times 10^4/\text{spill}$ . The  $\Sigma\text{tag}$  trigger rate was 140/spill and the total rate in the LS modules was 1200/spill. The average rate of the  $\Sigma\text{tag} \cdot \overline{E_{\text{cal}}}$  trigger after applying all of the beam vetoes was around 70 Hz.

As shown in Fig. 8(b), ADC and TDC data in each spill were accumulated in an auxiliary

CAMAC crate controller, named as List Sequencer. During the beam-off period, the data in the List Sequencer were transferred to a VME board computer through a CAMAC-VME interface. The data were then written to 8 mm magnetic tape, and 10% of the data were sent to another computer to monitor the data quality online.

### 3. Analysis

The photon detection inefficiency of the EM calorimeter due to photonuclear reactions

(INEFF<sub>cal</sub>) is determined from

$$\text{INEFF}_{\text{cal}} = \frac{N(E_{\text{cal}} < E_{\text{thresh}})}{N_{\gamma}} \cdot \frac{1}{\eta_{\text{LS}}}, \quad (1)$$

where  $N(E_{\text{cal}} < E_{\text{thresh}})$  is the number of LS-neutron events with an energy deposit in the EM calorimeter ( $E_{\text{cal}}$ ) below a specified threshold ( $E_{\text{thresh}}$ ),  $N_{\gamma}$  is the number of incident photons that are tagged, and  $\eta_{\text{LS}}$  is the neutron detection efficiency for the LS detector. The detection inefficiency, INEFF<sub>cal</sub>, is measured as a function of the incident photon energy,  $E_{\gamma}$ , and the calorimeter threshold  $E_{\text{thresh}}$ .

### 3.1. Calorimeter response

The incident photon energy,  $E_{\gamma}$ , is determined by the hit tagging counter with a small correction for the change in incident electron energy with the time in the beam spill [2,5]. For each calorimeter, an accurate energy calibration was made offline using these tagged photons to relate the ADC value to  $E_{\gamma}$ .

Typical  $E_{\text{cal}}$  distributions for the CsI-(I) calorimeter, measured by the  $\Sigma\text{tag}$  trigger and  $\Sigma\text{tag} \cdot \bar{E}_{\text{cal}}$  trigger with  $E_{\gamma} = 340 \pm 20$  MeV, are shown in Figs. 9(a) and (b). The  $E_{\text{cal}}$  distribution in Fig. 9(a) can be divided into three regions: the peak region around  $E_{\text{cal}} \simeq E_{\gamma}$ , the tail region with  $0 < E_{\text{cal}} < E_{\gamma}$ , and the region near  $E_{\text{cal}} = 0$  MeV. Events in the peak region correspond to EM showers. Events in the tail region are from photonuclear reactions and punch-throughs. Most events with  $E_{\text{cal}} \simeq 0$  MeV are mis-tags in which a tagging counter signal is not from a photon. The mis-tag rate, which is defined as the ratio between the number of events with  $E_{\text{cal}} < 1$  MeV and the total number of events in the  $E_{\text{cal}}$  distribution for each tagging counter, is less than 2% for most of the  $E_{\gamma}$  range. In Fig. 9(b), most EM showers with  $E_{\text{cal}} \simeq E_{\gamma}$  are suppressed by the  $\Sigma\text{tag} \cdot \bar{E}_{\text{cal}}$  trigger. When a neutron signal is required in the LS, the calorimeter signal is always in the tail region.

### 3.2. Neutron identification

Identification of low energy neutrons is based on the LS ADC signals and the TOF between the LS counters and the tagging counter.

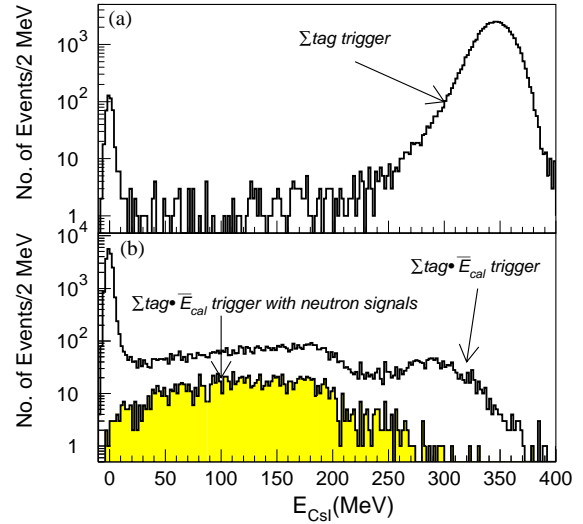


Fig. 9. Energy distribution in the CsI-(I) calorimeter for tagged photons at  $E_{\gamma} = 340 \pm 20$  MeV for (a)  $\Sigma\text{tag}$ -trigger events and (b)  $\Sigma\text{tag} \cdot \bar{E}_{\text{cal}}$ -trigger events. The shaded distribution is with a neutron signal requirement. Note that the  $\Sigma\text{tag}$  trigger is pre-scaled.

The first technique uses a difference between the signal pulse shapes for neutrons and photons, and has been widely used for neutron identification. For NE213 LS, neutrons generate a larger slow component of scintillation light compared with that by photons [7]. The pulse shape difference is obtained by measuring the ratio between two ADC values with different gate widths, 35 and 200 ns. The ADC value from the wide gate ( $Q_{\text{W}}$ ) corresponds to most of the total energy deposition. The ADC value from the narrow gate ( $Q_{\text{N}}$ ) corresponds mainly to the fast component of the scintillation signal. In this measurement, the relative timing between the LS analog signal and the ADC gate is critically important. To reduce time slewing as a function of pulse size, the starting time of each ADC gate was determined by a constant-fraction discriminator. A slight time skew still remains ( $\Delta\text{TOF}$ ), defined as the time difference between the true arrival time of a neutron into the LS detector and the start of the ADC gate. The time skew depends on the total signal charge,  $Q_{\text{W}}$ , as follows:

$$\Delta\text{TOF} \propto \frac{A}{\sqrt{Q_{\text{W}}}} - B \cdot Q_{\text{W}}, \quad (2)$$

where the first term proportional to  $A$  gives the pulse-height dependence, and the second term ( $B \cdot Q$ ) is a zero-level-shift effect due to the constant-fraction discriminator. The first term is the main component of the time skew. To correct the ADC value for gate-timing slew, we assume the scintillation pulse shape to be a triangle as shown in Fig. 10. The relation between the charges measured in the two gates is then

$$Q_N = Q_W \cdot \left(1 - \frac{X^2}{2 \cdot L1 \cdot L2}\right), \quad (3)$$

where  $X$  is the time difference between the end of the narrow gate and the end of signal pulse,  $L1$  is the total time duration of the signal pulse, and  $L2$  is the time difference between the peak and the end of the pulse (Fig. 10). Here,  $X$  depends on the gate timing which has the charge dependence described by Eq. (2). Substituting Eq. (2) into Eq. (3) gives the following relation between  $Q_N$  and  $Q_W$ :

$$Q_N = f(Q_W) \simeq \sum_{i=0}^4 C_i Q_W^{i/2} \quad (4)$$

where  $C_0$ – $C_4$  are five parameters to be determined for neutrons and photons separately. Although the  $C_i$  are algebraically related to the parameters in Eqs. (2) and (3), the  $C_i$  are determined instead from the data. Tight selection requirements on the  $Q_N/Q_W$  ratio and TOF are used to identify neutrons and photons (with poor efficiency), and then fit to Eq. (4) to determine the  $C_i$ . The measured  $C_i$  determine the functions  $f_\gamma(Q_W)$  and  $f_n(Q_W)$ , which relate  $Q_N$  and  $Q_W$  for photons and

neutrons, respectively. Finally we introduce an AUN (are you neutron?) likelihood:

$$\text{AUN} = \frac{f_\gamma(Q_W) - Q_N}{f_\gamma(Q_W) - f_n(Q_W)}. \quad (5)$$

Events with AUN near 1 are associated with neutrons, and events with AUN near zero are associated with photons. For each event, we determine the AUN likelihood from the measured  $Q_N$  and  $Q_W$  values. A typical AUN distribution is shown in Fig. 11(a). Two peaks corresponding to neutrons and photons can be clearly seen. To illustrate the improvement in using the AUN likelihood compared to a simple  $Q_N/Q_W$  ratio, we define a figure of merit (FOM) as

$$\text{FOM} \equiv \frac{\text{Peak}(n) - \text{Peak}(\gamma)}{\sqrt{\sigma(n)^2 + \sigma(\gamma)^2}}, \quad (6)$$

where  $\text{Peak}(n, \gamma)$  and  $\sigma(n, \gamma)$  are the peak positions and widths obtained by fitting with a Gaussian function for neutrons and photons, respectively. Using AUN we obtain  $\text{FOM} = 2.2$ ; using the  $Q_N/Q_W$  ratio we obtain  $\text{FOM} = 1.74$ . The improved FOM using the AUN likelihood shows the importance of the time slew correction in the ADC signal.

The second technique uses the TOF between the calorimeter and the LS counters. The TOF distribution measured with the  $\Sigma\text{tag} \cdot \overline{E_{\text{cal}}}$  trigger (Fig. 11(b)) has two peaks corresponding to prompt photons and to the slower neutrons. The correlation between AUN and TOF in the LS-2 counter is shown in Fig. 12 for the  $\Sigma\text{tag} \cdot \overline{E_{\text{cal}}}$  trigger, where LS-2 means 2nd-layer LS detectors as shown in Fig. 2. The “neutron” box shows the selection requirement for neutrons. The contribution from accidentals between the  $\Sigma\text{tag}$  trigger and the neutron signal is determined from the “accidental” box in Fig. 12.

### 3.3. Neutron detection efficiency

There is no direct method to determine the efficiency of the LS system for neutrons. We therefore rely on an indirect method based on the number of hits among the 12 LS counters.

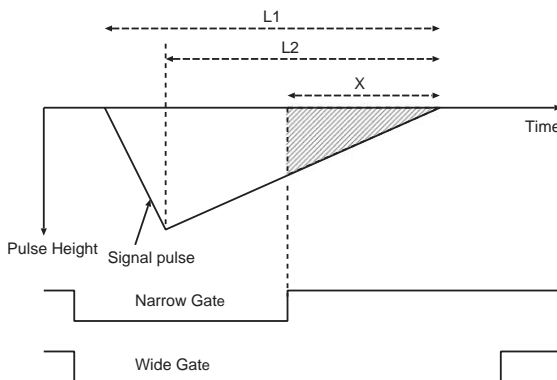


Fig. 10. Conception of correction for the time skew.

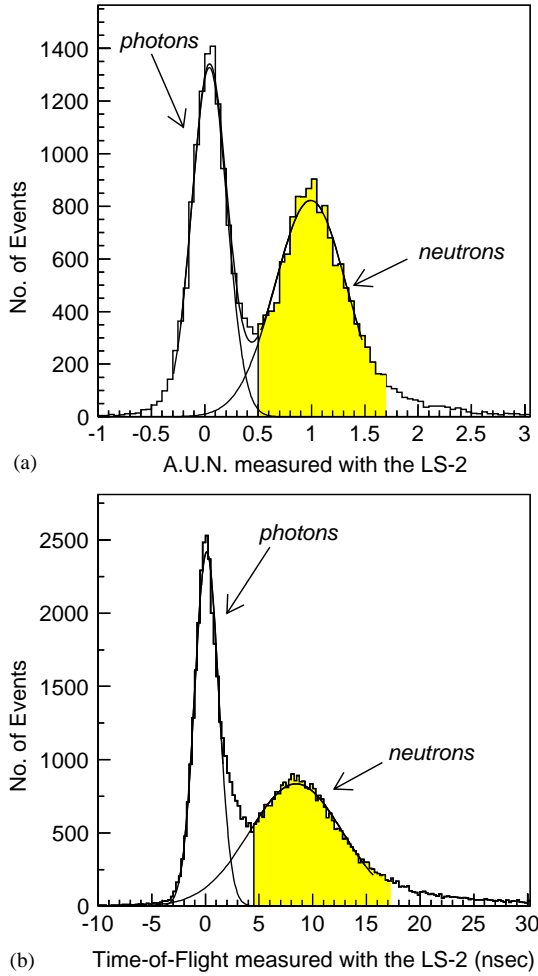


Fig. 11. Typical distribution of the “are you neutron” likelihood (AUN) and time-of-flight (TOF) measured by the 2nd LS in the  $\Sigma\text{tag} \cdot \bar{E}_{\text{cal}}$ -trigger. These data are from the SC-(I) lead-scintillator calorimeter and  $E_e = 750$  MeV. The shaded areas show the events selected as neutrons.

For each event, the number of LS detectors with a neutron signal is defined as the “multiplicity” ( $m_{\text{LS}}$ ), and the multiplicity ranges from 0 to 12. Typical neutron multiplicity distributions of the LS detectors are shown in Fig. 13 for the 1mm/3mm sampling calorimeter in the tail region ( $E_{\text{cal}} < 0.5 \cdot E_\gamma$ ). In general, the mean of number of neutrons emitted through evaporation process is around 10 or more for heavy nuclei like lead [8]. In our measurement, the probability of a neutron

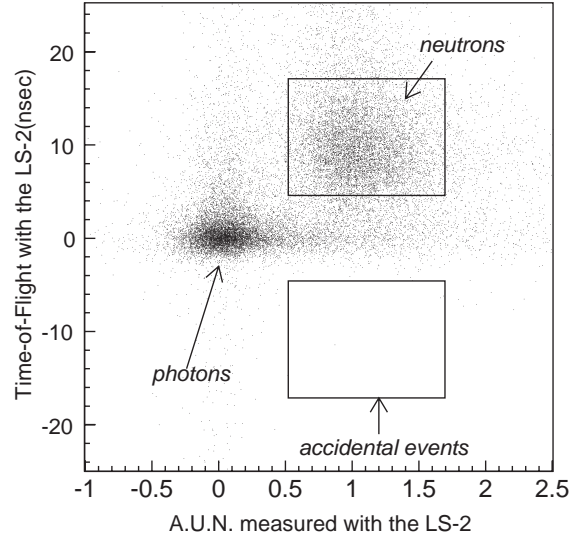


Fig. 12. Correlation between the “are you neutron” likelihood (AUN) and TOF for the  $\Sigma\text{tag} \cdot \bar{E}_{\text{cal}}$ -trigger events. These data are from the SC-(I) calorimeter and  $E_e = 750$  MeV.

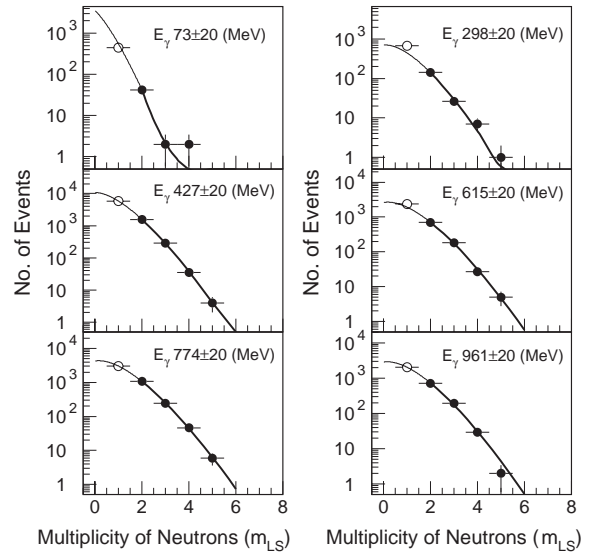


Fig. 13. Multiplicity distributions of neutron signals for SC-(I). The curves show the fitting results with Poisson distributions in the region greater than or equal to two ( $m_{\text{LS}} \geq 2$ ). In this fitting, we used closed circles for the fitting, and not used open circles.

detection by any individual LS detector is expected to be less than 15%, which includes geometrical acceptance, software selection and the interaction

cross section. Since the LS detection probability is small, the multiplicity distribution is well described by a Poisson distribution as shown in Fig. 13. The neutron detection efficiency ( $\eta_{\text{LS}}$ ) is defined in terms of a Poisson mean ( $\mu$ ) and a minimum multiplicity ( $m_{\text{LS}}^{\text{min}} = 1$  or 2):

$$\eta_{\text{LS}}(m_{\text{LS}} \geq 1) = 1 - P(0) = 1 - e^{-\mu} \quad (7)$$

$$\eta_{\text{LS}}(m_{\text{LS}} \geq 2) = 1 - P(0) - P(1) = 1 - e^{-\mu} - \mu e^{-\mu} \quad (8)$$

Events with  $m_{\text{LS}} = 1$  can be used to determine a Poisson mean, but these events must be corrected for accidentals. Therefore we use events with  $m_{\text{LS}} = 1$  only in cases with poor statistics.

The photon energy dependence of the Poisson mean ( $\mu$ ) is shown in Fig. 14 for events with  $m_{\text{LS}} \geq 1$  and also for  $m_{\text{LS}} \geq 2$ . The value of  $\mu$  increases from 0.2 at 100 MeV to 0.75 at 1000 MeV. No appreciable difference is observed between these two samples. We also check for a  $\mu$ -dependence on the energy deposition in the calorimeter. As shown in Fig. 15, there is no significant systematic dependence for  $0.05 < E_{\text{cal}}/E_{\gamma} < 0.45$ . Based on this observation, we assume that our efficiency determination is valid for  $E_{\text{cal}}/E_{\gamma} < 0.1$ .

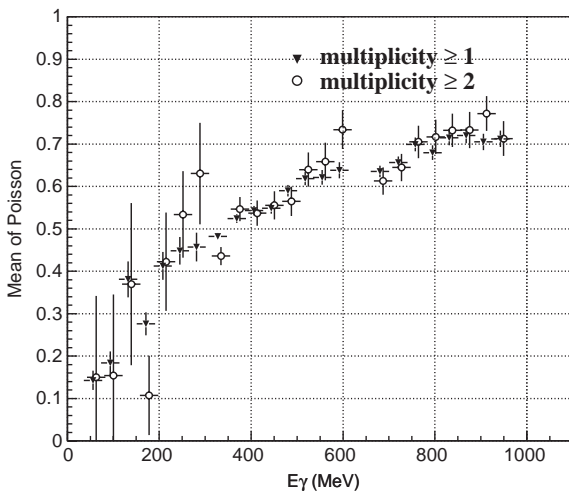


Fig. 14. Energy dependence of  $\mu$  for SC-(I) for two multiplicity regions,  $m_{\text{LS}} \geq 1$  (solid triangles) and  $m_{\text{LS}} \geq 2$  (open circles).

The  $E_{\text{cal}}$  distributions for the  $m_{\text{LS}} \geq 1$  and  $m_{\text{LS}} \geq 2$  samples are shown in Fig. 16. The shapes of the distributions are approximately the same, while the relative ratio depends slightly on the incident photon energy.

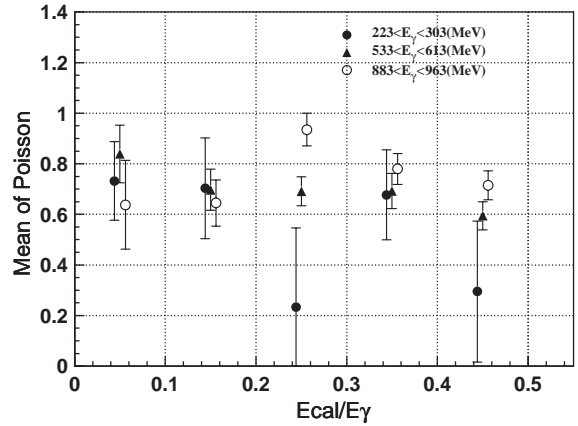


Fig. 15. Poisson mean  $\mu$  as a function of  $E_{\text{cal}}/E_{\gamma}$ , and as a function of incident photon energy. Fitting of the neutron multiplicity was performed in the region of  $m_{\text{LS}} \geq 2$ .

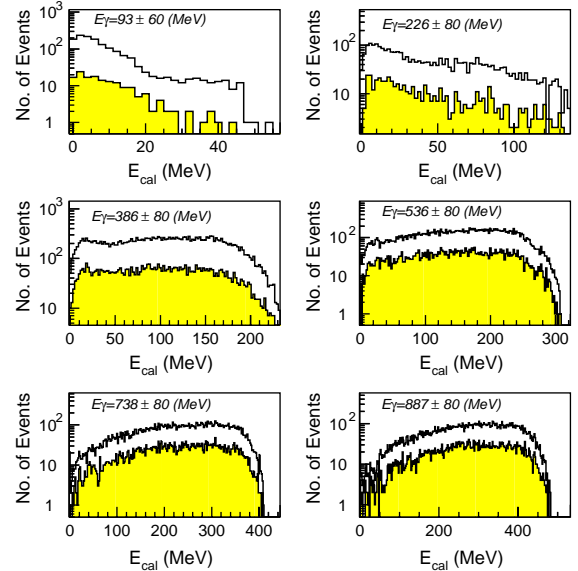


Fig. 16.  $E_{\text{cal}}$  distributions for SC-(I) with a neutron-signal requirement. The blank histograms are for events with  $m_{\text{LS}} \geq 1$ . The shaded histograms are for the events with  $m_{\text{LS}} \geq 2$ .

#### 4. Results and discussion

The photon detection inefficiency is determined from the relation given by Eq. (1). Results are shown in Figs. 17, 18 for CsI and lead-scintillator calorimeters, respectively, with  $E_{\text{thresh}} = 10$  MeV and  $m_{\text{LS}} \geq 2$ . Both figures show that the ineffi-

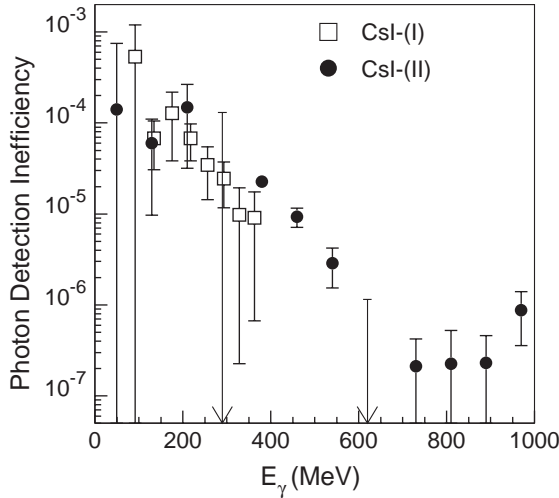


Fig. 17. Photon detection inefficiency due to photonuclear reactions for the undoped-CsI crystal calorimeters. The CsI energy threshold is 10 MeV. The arrows indicate 90%-confidence upper limits for the CsI-(II) inefficiency.

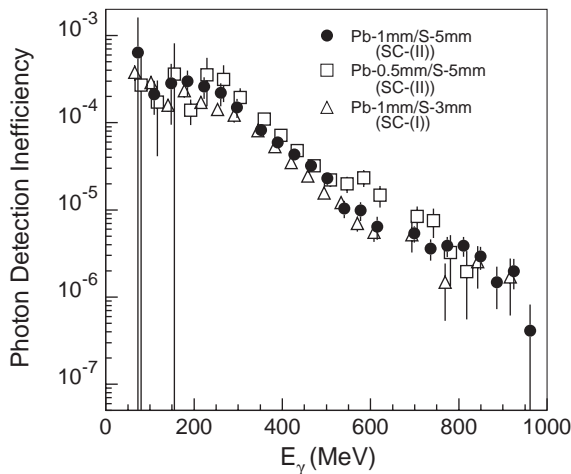


Fig. 18. Photon detection inefficiency due to photonuclear reactions for the sampling-type calorimeters. The energy threshold is 10 MeV.

ciency decreases as the photon energy increases with a shoulder near  $E_\gamma = 200$  MeV. For the CsI calorimeters, the inefficiency decreases from  $10^{-4}$  at  $E_\gamma = 200$  MeV down to  $2 \times 10^{-7}$  at  $E_\gamma = 1000$  MeV. There is no significant difference between the two CsI calorimeters. For lead-scintillator sandwich calorimeters, the inefficiencies are a factor of 2–3 larger than for CsI. The uncertainty at higher photon energies is dominated by the statistical error on  $N(E_{\text{cal}} < E_{\text{thresh}})$ . The uncertainty at lower photon energies is dominated by the error in the estimation of the neutron detection efficiency because of the smaller neutron multiplicity. Slight differences are observed among the inefficiencies for the three sampling configurations. This tendency is correlated with the value of  $\alpha$  (Table 2), the ratio between the number of nuclear-interaction lengths and the number of radiation lengths: the sampling configuration with smaller  $\alpha$  showing better results, that is, smaller inefficiencies.

Figs. 19 and 20 show the  $E_{\text{thresh}}$  dependence of the inefficiency for the CsI-(I) calorimeter and for the SC-(I) calorimeter at three detection thresholds,  $E_{\text{thresh}} = 1, 5$  and 10 MeV, respectively. In this case we use the data with  $m_{\text{LS}} \geq 1$  and subtract the contribution from accidentals. For both

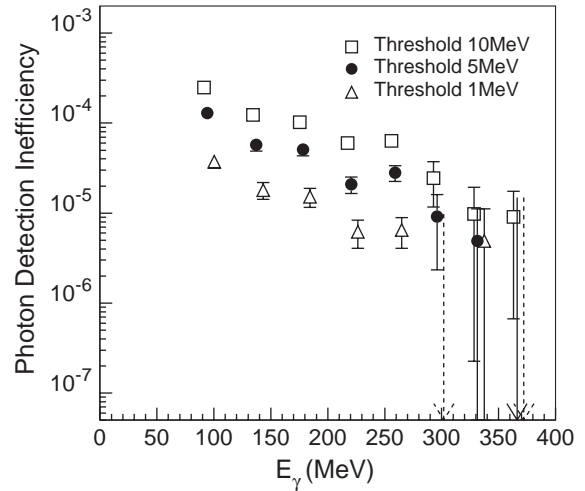


Fig. 19. Threshold energy dependence of the photon detection inefficiency due to photonuclear reactions for CsI-(I). The solid and dashed arrows indicate 90% confidence upper limits for energy thresholds of 5 and 1 MeV, respectively.

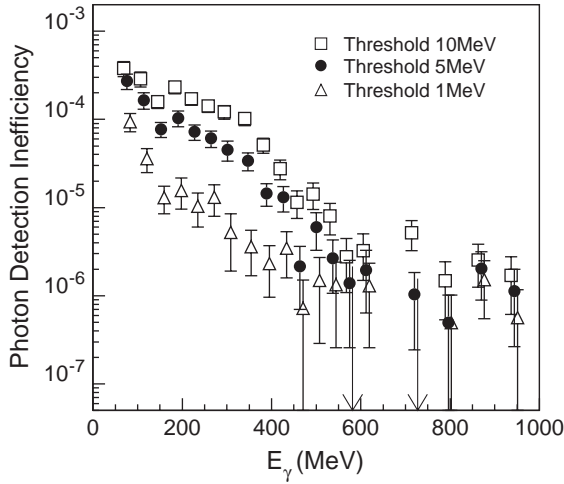


Fig. 20. Threshold energy dependence of the photon detection inefficiency due to photonuclear reactions for SC-(I). Arrows show the upper limit for the 1-MeV threshold case at the 90%-confidence level.

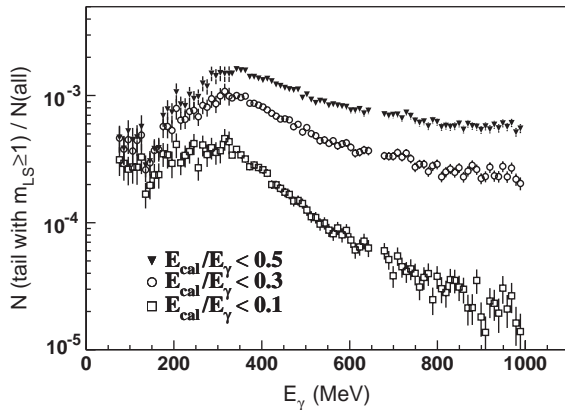


Fig. 21. Photon energy dependence of the ratio between the number of events in the tail region and the total number of incident photons. The tail events require a neutron signal in one or more LS detectors, and the ratio is corrected by the neutron detection efficiency.

calorimeters, the inefficiencies are appreciably reduced with lower energy thresholds.

The inefficiencies at higher thresholds are shown in Fig. 21 for the SC-(I) calorimeter, where the detection threshold is given by  $x = E_{\text{cal}}/E_{\gamma} = 0.1, 0.3$  and  $0.5$ . The  $E_{\gamma}$  dependence for  $x = 0.5$  shows a similar tendency with that of the photonuclear

cross section [9,10]. The curve for  $x = 0.1$  strongly declines at a higher photon energy, which implies that the event fraction of small energy deposition due to photonuclear reactions becomes much less in the higher photon energy region.

The present results for the CsI calorimeters are consistent with our previous results [2], but the inefficiency results for the current sampling calorimeters are smaller than our previous results by a factor of 10. One reason for the discrepancy could be the different sampling configurations; the previous calorimeter was a sandwich of 2-mm-thick lead and 6-mm-thick scintillator plates (denoted 2/6), compared to the current calorimeters with less lead per layer (1/5, 0.5/5, and 1/3). Another possible reason for the discrepancy is a difference in the neutron identification as explained in Section 2.3. Future experiments should pursue the discrepancies in the sampling calorimeters.

## Acknowledgements

The authors would like to thank the operating crew of the KEK-Tanashi 1.3-GeV electron synchrotron for their support throughout the experiment. This work was partly supported by a Grant-in-Aid for Scientific Research of the Ministry of Education, Science, Sports and Culture of Japan, and by the United States National Science Foundation.

## References

- [1] T. Inagaki, et al., Measurement of the  $K_L^0 \rightarrow \pi^0 \nu \bar{\nu}$ , KEK Internal 96-13 (1996).
- [2] S. Ajimura, et al., Nucl. Instr. and Meth. A 435 (3) (1999) 408.
- [3] W.R. Nelson, H. Hirayama, D.W.O. Rogers, SLAC Report 265, 1985.
- [4] S. Arai, et al., Jpn. J. Appl. Phys. 14 (1975) 95.
- [5] M. Mutoh, J. Sci. Hiroshima Univ. 51 (1987) 187.
- [6] R.S. Kessler, et al., Nucl. Instr. and Meth. A 368 (1996) 653.
- [7] F.J. Lynch, et al., IEEE Trans. Nucl. Sci. NS-431 (1975) 58.
- [8] R. Madey, et al., Phys. Rev. C 25 (1982) 3050.
- [9] P. Carlos, et al., Nucl. Phys. A 431 (1984) 573.
- [10] S. Eidelman, et al., Phys. Lett. B 592 (2004) 1.